From CO_2 to solid carbon: reaction mechanism, active species, and conditioning the Ce-alloyed GaInSn catalyst

Daniel Lörch,[†] Aya G.A. Mohamed,[‡] Holger Euchner,[†] Janick Timm,[†] Jonas Hiller,[†] Peter Bogdanoff,[‡] and Matthias M. May[*,†]

[†]*Universität Tübingen, Institute of Physical and Theoretical Chemistry, Tübingen, Germany*

[‡]*Helmholtz-Zentrum Berlin für Materialien und Energie, Institute for Solar Fuels, Berlin, Germany*

E-mail: matthias.may@uni-tuebingen.de

Abstract

The electrochemical reduction of CO_2 is a promising realisation of negative emissions to mitigate climate change, aiming at the efficient production and safe longterm storage of carbon-rich sink products. This approach, however, necessitates novel catalyst materials specifically targeting electrochemical carbon dioxide removal. In this work, we investigate synthesis routes for a cerium-incorporated GaInSn-based liquid metal catalyst, focusing on the electrochemical production of graphitic carbon. Preparation and preconditioning of the catalyst are found to be crucial for carbon production, while trace amounts of H_2O and OH in the organic electrolyte play a decisive role for the efficiency of the electrocatalytic process. Finally, for a better understanding of the reaction mechanism and the involved active species, experimental findings and density functional theory-based calculations are combined, suggesting a two-step reduction pathway with $Ce(OH)_x$ as the catalytically active surface species.

Introduction

Apart from a drastic cut in emissions by the (full) transition from fossil to renewable energies, the disposal of CO_2 from the earth's atmosphere – so-called negative emissions or carbon dioxide removal (CDR) – is likely to become a challenge, mankind has to face within the next decades, that is associated with significant land conversion.[1,2] In this context, realising these negative emissions at scale is becoming an increasingly important research topic spanning a variety of research fields.[3,4] A large number of currently investigated CDR-technologies are based on biological pathways or on a direct injection of CO_2 into underground reservoirs.[3,5] (Photo-)electrochemical methods – often also referred to as artificial photosynthesis – offer a different approach. Here, solar light is used directly or indirectly by an artificial, light-absorbing structure to convert CO_2 into long-term stable, storable products via a thermodynamically uphill electrochemical reaction. This allows in principle for much higher efficiencies than natural photosynthesis, thus drastically reducing the land-footprint of this

method as well as the competition for arable land and water.[6,7] While artificial photosynthesis is more often highlighted for producing value-added products such as solar fuels,[8] there is a growing recognition of its importance in the efficient and permanent removal of CO_2 from the atmosphere and its conversion into stable storage products. An ideal storage product should be long-term stable, with the underlying process showing a high solar-to-carbon (STC) efficiency,[6] where the latter does not depend on the stored energy. This typically excludes the formation of energy-rich C-H bonds, as for instance in methane or alcohols. Consequently, storage products of interest range from liquids, such as formic or oxalic acid brines, to solid products, such as carbon flakes. The first step for such solar-driven CDR is to find suitable electrocatalysts, which can then be integrated in a number of ways with a solar absorber to finally assess the STC of a given system.

Liquid metal-based catalysts have recently been suggested to open a promising route towards the production of solid carbon via electrochemical CO_2 reduction.[9–11] However, so far only a small number of studies exists, leaving the underlying mechanism still unclear. This has resulted in contradictory hypotheses, which also seem to be caused by unidentified or undisclosed parameters in the synthesis process of the respective catalysts.[9–11] Ga-based liquid metals are promising catalyst candidates, since they enable an operation at low temperatures, while maintaining their liquid properties. Additionally, they show excellent anti-coking behaviour, as solid products adhere poorly to liquid interfaces and detach easily. The most frequently used materials, especially with respect to the formation of solid carbon, are either GaIn or GaInSn, both of them enabling room temperature experiments.[12,13] The latter is often referred to with the trade-mark name "Galinstan". This however, does not clarify whether the eutectic GaInSn composition is at use (Ga: 68.5 wt.%, In: 21.5 wt.%, Sn: 10 wt.%) or a technical grade, which may also include fluxing agents or other additives and thus may change the physio-chemical and catalytic behaviour significantly.[14]

When it comes to the formation of solid carbon from CO_2 in an electrochemical setup, several metals, such as cerium, vanadium or lithium, have been shown to act as (co-)catalyst,

when incorporated in a liquid metal matrix.[10,11] At this stage, a direct comparison between studies is challenging, as e.g. the description of the catalyst and its synthesis frequently lacks detail with respect to either the catalyst preparation steps, the quantity of the actual catalyst, the LM composition or the potential role of detected contaminants.[9,10] Furthermore, a detailed understanding of the underlying processes is currently still missing, as the proposed mechanisms are essentially limited to a somewhat speculative reaction equation level and so far do not elaborate further into an interfacial analysis. Hence, there is a clear need for further, in-depth investigations of this liquid metal-based catalyst type for CO_2 reduction to solid carbonaceous products.

In this work, we aim to contribute to the understanding of this electrochemical reaction mechanism by focusing on the GaInSn-cerium system. For this purpose, we first investigate eutectic GaInSn for its electrocatalytic activity with respect to CO_2 reduction. For pure GaInSn, already a certain catalytic activity is observed, whereas the addition of Ce results in slightly increased current densities and the yield of solid products with increased carbon content. While these results are in partial agreement with previous work on Ce-alloyed GaInSn,[9–11] we furthermore investigate the underlying reaction mechanism, pointing particularly towards the importance of water or hydroxyl concentrations in the electrolyte and shedding light onto the relevant surface species and intermediate products of the overall mechanism. Such an improved understanding with respect to synthesis and reaction mechanism will help to more reliably asses the performance of the electrocatalyst, also in a solar-driven approach. Moreover, an understanding of the electrocatalytic process will allow for tailoring improved materials with improved catalytic efficiencies.

Methods

Sample preparation

GaInSn with a stoichiometry of $Ga_{0.784}In_{0.149}Sn_{0.067}$ (68.5:21.5:10 weight %), was purchased from Goodfellow (>99.8 %). To allow for CO_2 reduction aiming at carbonaceous products, GaInSn was alloyed with small portions of cerium, such that the resulting alloy contains 1 wt% of cerium. It has to be pointed out here that the alloying process – sometimes also referred to as *doping* – faces the challenge that cerium is immediately covered by an oxide layer. This even occurs in nitrogen environments with oxygen levels of < 2 ppm, and prevents a proper incorporation of cerium in the liquid metal if the oxide layer is not removed or mechanically broken. During the alloying process, cerium atoms are dissolved in the GaInSn matrix while, due to the small dissolution limit, metallic Ce nanoparticles also remain present (see Fig. 1). The mechanical incorporation of commercial Ce nanoparticles in GaInSn by grinding both components in a mortar has first been described by Esrafilzadeh et al.[9]. However, we found that additional process steps have to be followed in order to reliably and reproducibly incorporate cerium in the GaInSn matrix. The first process step is the preconditioning of mortar and pestle, by alternating treatment of their surfaces with 1 M HCl (Merck, 32 %) and 1 M KOH solution (Merck, > 99.9 %), followed by grinding of pure GaInSn at ambient conditions. This results in the development of a native oxide layer on the LM droplet which makes the latter loose its surface tension and hence its spherical shape, thus allowing it to be spread out on a surface.[15] Once pestle and mortar were fully covered with GaInSn, they were transferred to a glovebox with N_2-atmosphere and the excess GaInSn was removed from the mortar, such that only a mirror-like skin layer remained. In the glovebox, a defined amount of GaInSn was added to the mortar, which directly spread out due to the interaction with the skin layer. Only after this step, the mechanical incorporation of additional elements could proceed. This is due to the fact that inflicting any forces on the pestle-surface/additive/GaInSn-droplet/mortar-surface system is impossible for a spherical

liquid metal droplet, thus making a mechanical alloying process unfeasible. The second adjustment was the preparation of cerium metal flakes inside the glovebox by chipping or filing down a high-purity cerium foil (Thermo Fisher Scientific, 99.9 %) just before weighing and adding it in small aliquots to the GaInSn during the actual alloying process in the N_2-glovebox. By following that procedure, larger flakes with a lower relative amount of surface oxides were produced. This limits the risk of oxidized nanoparticles forming a coherent layer on the LM surface which otherwise can lead to the reformation of coherent spherical droplets, sometimes referred to as "liquid metal marbles" that again prevent the infliction of the force necessary for alloying.[16] The successful alloying was checked with scanning electron microscopy (SEM) and energy-dispersive X-ray spectroscopy (EDX) (cp. Fig. 1).

Electrochemical setup

The setup for electrochemical measurements has to address the specific requirements resulting from the liquid nature of GaInSn. To solve challenges such as electric contact loss of the liquid metal droplet due to capillary and electrostatic forces as well as locomotion,[17] a specific electrochemical cell was constructed (see Fig. 2). The contacting of the GaInSnCe droplet was realised by using a previously GaInSn-coated copper foil (Thermo Fisher Scientifc, $>99.95\,\%$) as a mount, on which the GaInSnCe catalyst was deposited as depicted in Fig. 1(d). The coating process leads to the formation of a Ga_xCu_y alloy that enables the GaInSnCe droplet to wet the foil. Finally, the mount was contacted from the back via a pressing-contact. If not stated otherwise, an electrolyte solution consisting of Dimethylformamide (DMF, Thermo Fisher Scientific, $>99.5\,\%$) | 2 M H_2O | 0.1 M Tetrabutylammonium hexafluorophosphate ($TBAPF_6$, Merck, $>99.0\,\%$) was used during the electrochemical experiments. To ensure low amounts of residual H_2O in the chemicals, the DMF was stored over activated molecular sieves (4 Å, VWR BDH Chemicals) and the $TBAPF_6$ was stored in a vacuum desiccator prior to use. The H_2O in use was drawn from a Milli-Q purification system. As counter electrode, a Pt-coil (Thermo Fisher Scientific, 99.9 %) was used, that was

(a)

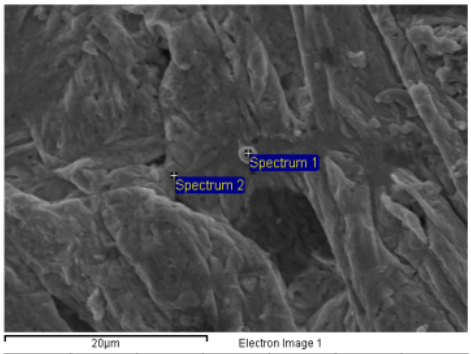

Spectra	O	Si	Ga	In	Sn	Ce
Spec 1	17.45	3.07	61.61	11.54	5.34	0.99
Spec 2	12.74	2.63	65.6	12.36	5.56	1.11

(b)

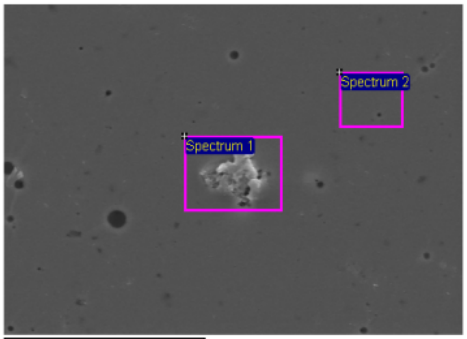

Spectra	O	Si	Ga	In	Sn	Ce
Spec 1	11.74	1.29	66.93	10.34	4.65	5.06
Spec 2	-	1.45	76.44	15.45	6.66	-

(c)

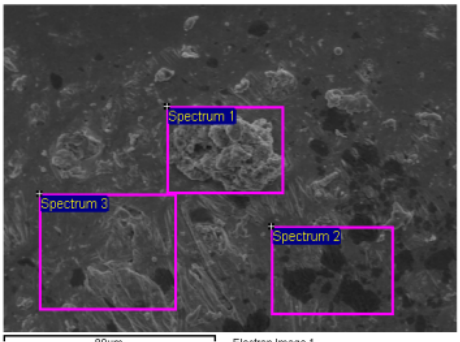

Spectra	C	O	Si	Ga	In	Sn	Ce
Spec 1	5.43	6.64	1.13	53.57	8.81	4.6	19.82
Spec 2	7.55	1.95	0.7	60.63	18.17	8.79	2.22
Spec 3	-	2.19	1.05	64.38	20.15	9.94	2.3

(d)

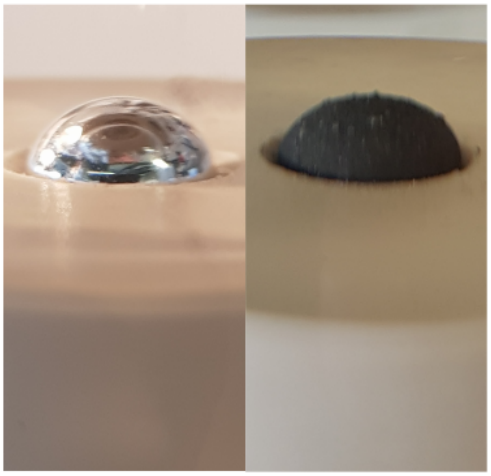

Figure 1: SEM images and atomic ratios (EDX) of three different GaInSnCe batches. (a) Alloying procedure according to method section; (b) alloying procedure according to literature;[9] (c) GaInSnCe after chronoamperometry at -2.6 V vs. $Ag/AgNO_3$, from the same batch as (a); (d) photos of a GaInSnCe droplet in the electrochemical setup before and after the electrochemical experiments.

separated from the main electrolyte solution volume by a glass frit. As reference electrode system, a RE-7N reference electrode from ALS was filled with a 0.1 M $TBAPF_6$ and 0.01 M $AgNO_3$ (Merck, $>99.8\,\%$) acetonitrile solution. If not stated otherwise, chemicals were used without further purification.

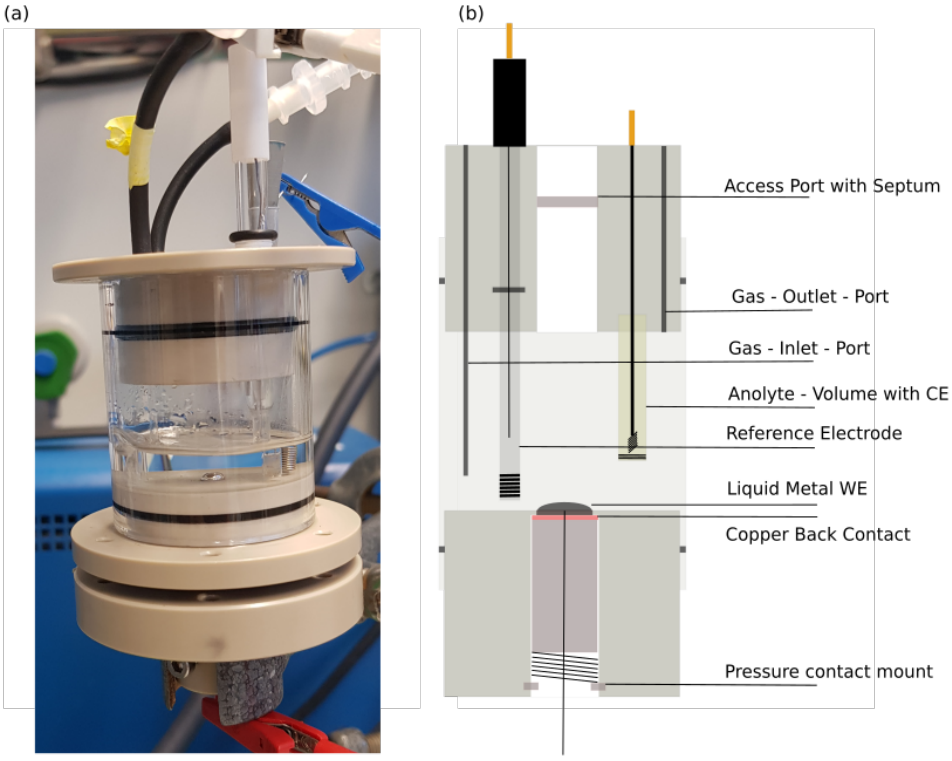

Figure 2: Electrochemical cell developed for measurements on a liquid metal electrode. (a) Photo of the cell under operating conditions, (b) schematic drawing of the cell design (sectional view).

Electrochemical characterisation

The electrocatalytic processes on the LM were investigated by cyclic voltammetry (CV), using an AMEL 2551 potentiostat with the software VApeak2017 v3. The CV experiments were performed with a scan rate of 50 mV/s and the potential was cycled five times between -1 and -3 V vs. $Ag/AgNO_3$. Before conducting the CVs, the electrolyte solution was purged with the respective gas (N_2 or CO_2 (Westfalen, 99.999 %)) for 30 min. To gain insights in the influence of incorporated cerium on the electrochemical process, CVs and chronoamperometry (CA) measurements were performed with either pristine GaInSn or alloyed GaInSnCe as working electrode. The experiments were conducted with the dry electrolyte solution or with small amounts of H_2O added to the solution. Finally, the pH of the H_2O was adjusted by ei-

ther adding 1 M HCOOH (Merck, 89-91 %) or 1 M KOH. To normalise the resulting currents, the effective area of the working electrode was estimated by assuming it to be a spherical segment. Thus, the area could be calculated according to the equation $M_{h,a} = \pi\,(a^2 + h^2)$, with a (radius of the cap-base) and h (height of the cap) as determined from pictures taken during the experiment that were processed with the software Image-J.[18]

Electrode characterisation and product analysis

For XPS characterisation, a non-monochromated Al K_α source was used in a ultra-high vacuum chamber with a base pressure of $\leq 5 \cdot 10^{-9}$ mbar. The system was equipped with a Phoibos 100 MCD analyzer from SPECS. Survey scans were taken at a pass energy (E_{pass}) of 50 eV, while for detail scans, 20 eV were applied. Binding energies were calibrated using the metallic component of the Ga $2p_{3/2}$ peak, setting its binding energy to 1116.7 eV, while for the Ce metal sample, the binding energy of the metallic Ce $3d_{3/2}$ peak was set to 900.56 eV.

For SEM measurements, a JEOL JSM-6500F with schottky emission electron gun was used in combination with an Oxford INCA Energy 200 EDX system. The scans presented here were taken at an acceleration voltage of 15 kV.

Raman spectra were recorded using a home-built, inverted confocal laser stage scanning microscope. A narrow-linewidth 532 nm (2.33 eV) diode laser was used for excitation. The signal was recorded by an Andor DU4A01-BVF camera attached to an Andor SR-303i-B spectrometer, using a 1200 g/mm diffraction grating. Prior to the measurements, the instrument was calibrated using a Neon gas-discharge lamp. The temperature of the camera was kept constant at -60 °C. An infinity-corrected 100x/1.4 NA oil immersion objective was used to focus the excitation laser to a diffraction-limited focal volume and collect the scattered radiation. The samples consisted of drop-cast films of the material on a glass coverslip and were investigated under ambient conditions. Two RazorEdge Long Pass E-Grade 532 filters were employed to exclude the signal below 100 cm^{-1}, thereby removing the laser-line.

For the analysis of the solid product obtained during the longterm experiments, we separated it from the LM matrix by scraping-off the topmost layer. This material was washed with acetonitrile and treated in a vortex shaker, leading to the separation of the remaining LM and the solid product. The hereby formed LM drop was withdrawn from the emulsion and finally, the slurry was stepwise dropcasted on Si wafers, dried first at ambient conditions in a fumehood, and finally in a drying cabinet at 60°C over night.

The electrochemically produced gases were analysed using gas chromatography (GC, Trace 1300, ThermoFisher) with a thermal conductivity detector. The GC was equipped with Restek columns (1 m, 5 Å molecular sieve 80/100 and 2 m Hyyesep Q 100/120) using argon as carrier gas. The electrochemically produced liquids were analysed using ion chromatography (IC, Metrohm AG, Switzerland) with a conductivity detector (930 Compact IC Flex) operated by MagIc-Net software. The eluent was 3.2 mM Na_2CO_3 + 1.0 mM $NaHCO_3$ + 16% acetonitrile, flowing through a 4 mm column Metrosep A Supp 7 - 150/4.0.

Computational

Periodic density functional theory (DFT) as implemented in the plane wave code VASP, was applied to investigate potential reaction mechanisms for the CO_2 reduction.[19,20] After optimizing the Ce bulk structure, a 3×3 supercell of the (111) surface was created, using a 5-layer slab with 15 Å vacuum on top. On this surface, the CO_2 reduction to CO and carbon was studied, also investigating the impact of co-adsorbed hydroxyl groups and trace amounts of water. All calculations used the projector-augemented wave (PAW) approach, while exchange and correlation where described by the RPBE functional in combination with the Grimme-D3 correction.[19,21,22] A plane-wave cutoff of 520 eV and a $4 \times 4 \times 1$ Γ-centred k-point mesh were applied.

Results and Discussion

Effects of electrolyte composition and alloying

In order to improve the understanding of the Ce-based CO_2 reduction mechanism as described in the literature,[9] experiments were designed and conducted that initially followed the originally suggested procedure. However, due to reproducibility issues with the originally proposed alloying procedure, the above-described, adjusted process was developed, leading to successful alloying and reproducible electrochemical measurements.

From the non-negligible current densities observed in the cyclic voltammograms performed in the CO_2-purged electrolyte (Fig. 3a), we deduce that both the pure GaInSn and the cerium-containing alloy are active towards carbon dioxide reduction, yet the former is in disagreement with the findings of Esrafilzadeh et al.[9]. The onset of the faradaic process - defined as the potential at - 100 $\mu A/cm^2$ - is slightly shifted towards less cathodic potentials (from -2.39 to -2.25 V vs. $Ag/AgNO_3$) when switching from a pure GaInSn to a GaInSn-Ce electrode in the electrolyte solution containing 2 M H_2O (Fig 3a, red curve). For the LM-Ce electrode in combination with the dry electrolyte solution, on the other hand, the onset is shifted to -2.49 V (Fig 3a, blue curve). The catalyst prepared according to the literature process, starting with Ce powder, shows an earlier onset at around -2.04 V (violet curves). However, a reduction wave with a maximum at -2.18 V seems to overlap with the faradaic process occurring at higher potentials. As it was not investigated whether the reduction wave is really linked to the CO_2 reduction process (e.g. CO_2 adsorption) or originates from alternative processes like the reduction of surface oxides, assigning the onset of -2.04 V to the CO_2 reduction does not seem justified.

The control experiments with the Ce-containing alloy under nitrogen-purged electrolyte solution in the absence of additional water (black curve) indicates that the faradaic process at cathodic potentials more negative than -2 V is linked to the CO_2 reduction, as the cathodic current is entirely missing in the absence of CO_2. And indeed, the main products in the

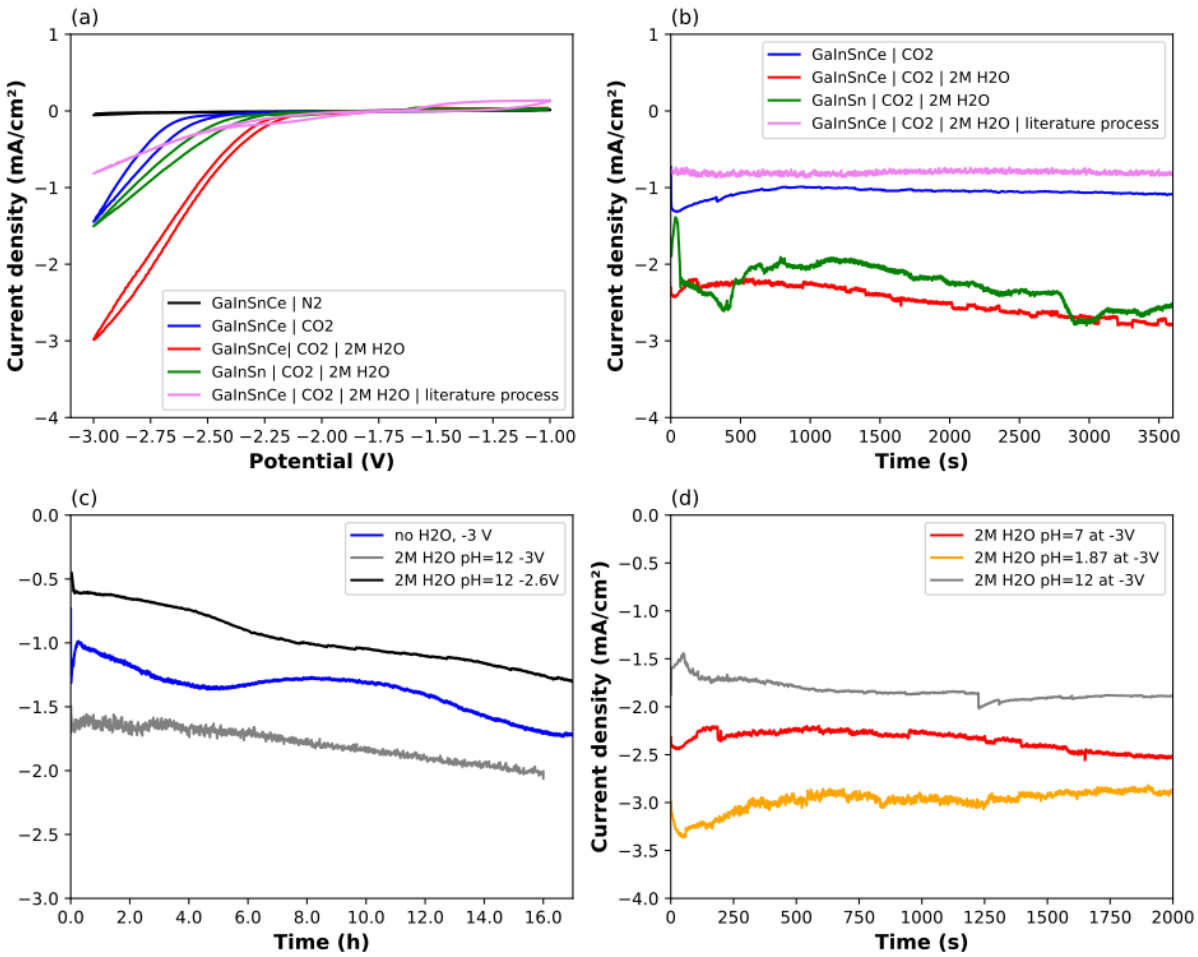

Figure 3: Electrochemical experiments on pure GaInSn and the Ce-containing alloy GaInSnCe. (a) Cyclic voltammetry in dependence of purging gas (CO_2 or N_2, black and blue curve) and H_2O content (red and green curves), (b) current density at -3 V vs. $Ag/AgNO_3$ for samples from (a), (c) longterm experiments at different potentials and electrolyte conditions, (d) current density at -3 V at different pH of the added H_2O.

process are carbon monoxide and – if H_2O is present at relevant amounts – formate as well as hydrogen as shown in Tab. 1. Small contributions to the cathodic current at potentials more cathodic than -2.7 V probably originate from the degradation of the conductive salt $TBAPF_6$, as its stability window suggests a decomposition at potentials more cathodic than -2.7 V.[23] At this point it should also be mentioned that a decomposition mechanism of the Tetrabutylammonium cation in DMF has been described for potentials lower than -2.7 V, which could in principle affect our results. However, as H_2O is described to strongly suppress

this effect, we regard it as negligible in comparison to the CO_2 reduction reaction.[24] To account for those effects, we mainly focus on electrolyte solutions containing H_2O in the following, and additional longterm experiments were conducted at -2.6 V vs. $Ag/AgNO_3$.

In Fig. 3(b), the evolution of the current density over the course of 1 hour of continuously applied potential (-3 V vs. $Ag/AgNO_3$) is depicted. The current density with pure GaInSn and the LM-Ce are similarly high ($\sim$2 mA/cm^2), with both of them slightly increasing during the experiment. Unlike in the case of the LM-Ce alloy, the current density with pure GaInSn seems to stop increasing at roughly -3 mA/cm^2. Furthermore, the evolution of the current density is more unsteady - possibly due to contacting issues. For the Ce-containing alloy, the absolute value of the current density is slowly increasing over time without reaching saturation in the observed time span. This holds for the case of a controlled amount of added H_2O as well as for the dry electrolyte, whose current densities start off at ca. -2.2 mA/cm^2 and -1 mA/cm^2, respectively. This ongoing increase becomes more apparent in the longterm experiments that are depicted in Fig. 3(c). During the extended CA measurement, a blackish surface evolves on the LM-Ce electrode alongside this gradual increase in current density (Fig. 1d). This does not occur in the case of the pristine GaInSn. Upon closer inspection during the experiment, it can be seen that this growth-process starts from multiple nucleation centres and proceeds to grow into larger flakes, ultimately covering the whole LM surface with a dense, opaque-blackish layer.

In the case of the water-containing setup, the three–dimensional growth of the blackish, solid product flakes proceeds more slowly than in case of the dry electrolyte solution. However, unlike for the dry electrolyte solution, the growth does not appear to come to a hold. Overall, the yield of the solid product is therefore more pronounced for the H_2O-containing electrolyte solution. Consequently, this suggests that controlled amounts of water impact the growth process and its kinetics significantly. Interestingly, this growth process is in both cases (dry and 2 M H_2O) accompanied by a slow increase in current density even after running the experiment for >16 h (see Fig. 3c). This could indicate a slow conditioning process

regarding the solid-liquid interface of the working or counter electrode, facilitating existing or enabling new reaction pathways. Another explanation might be, that the continuously growing amount of solid product deposited on the LM might show catalytic activity towards CO_2 reuction by itself, as it has been reported for graphite.[25] An increased hydrogen formation due to deposited product, on the other hand, is unlikely since the slope of the current density increase in case of the dry electrolyte solution is similar to the electrolyte solution with the added amount of H_2O. After periods longer than 10 h of constantly applied potential, the uppermost layers of the new surface starts to exfoliate. However, this does not hamper the catalytic process.

In contrast, the results were more ambiguous if the alloy was produced according to the procedure described in the literature Esrafilzadeh et al.[9] starting from Ce powder and a non-coated mortar. In Fig. 3(a) and (b), the typically encountered behaviour is depicted in violet. Overall, the current density is significantly lower when compared to the alloy prepared with our process. Furthermore, no observable amount of solid product was deposited on top of the alloy over the course of the experiment. When monitoring the resulting current densities in the potential range between -1 and -1.6 V as well as between -1.75 and 2.5 V, it can be observed that they are significantly more pronounced compared to our process. If the latter observation is linked to the presence of larger amounts of oxides in the final alloy, that are being reduced and oxidised repeatedly, this would point out the importance of a reliable alloying process that is independent of the actual technique of the operator as otherwise, the LM alloy is left in an ill-defined state.

To investigate the influence of acidity and alkalinity of the added water on the electrochemical behaviour and performance of the catalyst, the pH of the added H_2O was adjusted to 1.87, 7, and 12, respectively. Fig. 3(d) depicts the resulting current density of GaInSnCe at -3 V for these three different cases. While in all three experiments, an initial drop in current density is observable, the current density subsequently recovers without reaching saturation in case of alkaline (grey) and neutral (red) H_2O (see Fig. 3d). Alongside these differences in

current density over time, the growth of the blackish solid product also proceeds differently. In fact, first flakes of the solid product were visually observed after ∼120 s with alkaline H_2O, while they appeared only after about 1200 s with neutral H_2O. In the case of the acidified H_2O, no solid product was observed at all during the experiment. Consequently, the addition of H_2O increases the cathodic current at a given potential, while an increased pH H_2O promotes the CO_2 reduction yield towards the solid product.

As H_2O and, more specifically, the pH of the H_2O appear to have an impact on the formation of the solid product and the electrochemical performance overall, it should be mentioned that the solvation state of DMF/H_2O solutions is an ongoing research topic. However, there is the hypothesis that the supposedly homogeneously distributed DMF/H_2O system[26] obtains a microheterogeneity upon the addition of alkali cations due to the replacement of the H_2O in the DMF-n-H_2O structure.[27–29] Thus, we assume that by adding H_2O containing KOH, we create these microheterogeneities and consequently deal with a solvent of distinct H_2O- and DMF-microclusters (see discussion in SI).

Depending on the reaction mechanism, solid carbon formation from CO_2 may involve CO as an intermediate product or not.[30,31] To check for the hypothesis of CO as intermediate, we conducted experiments with the same electrolyte solution purged with CO (Westfalen, 99.97 %) instead of CO_2. This resulted in significantly lower and slowly decreasing current densities (Fig. S3b). However, the blackish product still evolved. Although the initial formation of the solid product seemed to occur faster than in the case of carbon dioxide, its further growth on the catalyst seems to come to a stop after ∼1-2 h (Fig. S3). This suggests that either the growth into larger graphitic carbon flakes is promoted by the presence of CO_2, or the catalyst deactivation is prevented. This could be linked to proton availability and we therefore analysed the reaction products by means of gas and ion chromatography.

Product analysis

Co-evolution of different products, with their relative ratios varying for catalyst and electrolyte composition, applied potential as well as with time, is a typical challenge for electrochemical CO_2 reduction.[32] We therefore evaluated the faradaic efficiencies (FE) for the main gaseous and dissolved products -– namely CO, H_2, formate and oxalate – after 1 h of potentiostatic experiment. Every 10 min, a head-space sample was analysed via gas chromatography. The mean values from these six measurements are given in Tab. 1. For the dissolved liquid products, the accumulated amount was determined by ion chromatography after the experiment was terminated. We find that the main product for the dry electrolyte is carbon monoxide, while the presence of H_2O leads to the additional formation of hydrogen and formate. In both cases, minor contributions of oxalate are measured. Over the "short" period of those experiments, a reliable quantification of the solid blackish product could not be conducted due to the small yield of the product.

Table 1: Faradaic efficiencies, η_F, of the gaseous and dissolved products during 1 h of applying -3 V to the Ce-containing GaInSn alloy in an electrolyte solution that is either dried or contains 2 M H_2O at pH 7.

η_F **for**	**GaInSnCe w/o** H_2O	**GaInSnCe with 2 M** H_2O
CO	93 ±1.32	36.9 ±1.24
H_2	0.7 ±0.85	21.0 ±1.29
$HCOO^-$	3.0	46.8
$C_2O_4^{2-}$	1.5	0.35
Sum	**98.2**	**105.1**

SEM/EDX analysis (Fig. 4a) shows that the separated mixture of solid product and catalyst falls into two main particle size categories. The first category ranges from roughly 1 to 3 μm diameter, while the second one is larger by an order of magnitude ranging from ∼10 to 30 μm. The atomic composition of category 2 (spectrum 2 and 3), which is generally spherically shaped, is in good agreement with the original composition of GaInSn. Category 1, on the other hand, is unevenly shaped, with roughly half of the signal stemming from the Si wafer (see spectrum 1). Slightly below 30% of the atomic species once again originate from

GaInSn residues with a pronounced Ga surplus. However, for this domain, an additional signal emerges, corresponding to ∼13 % carbon.

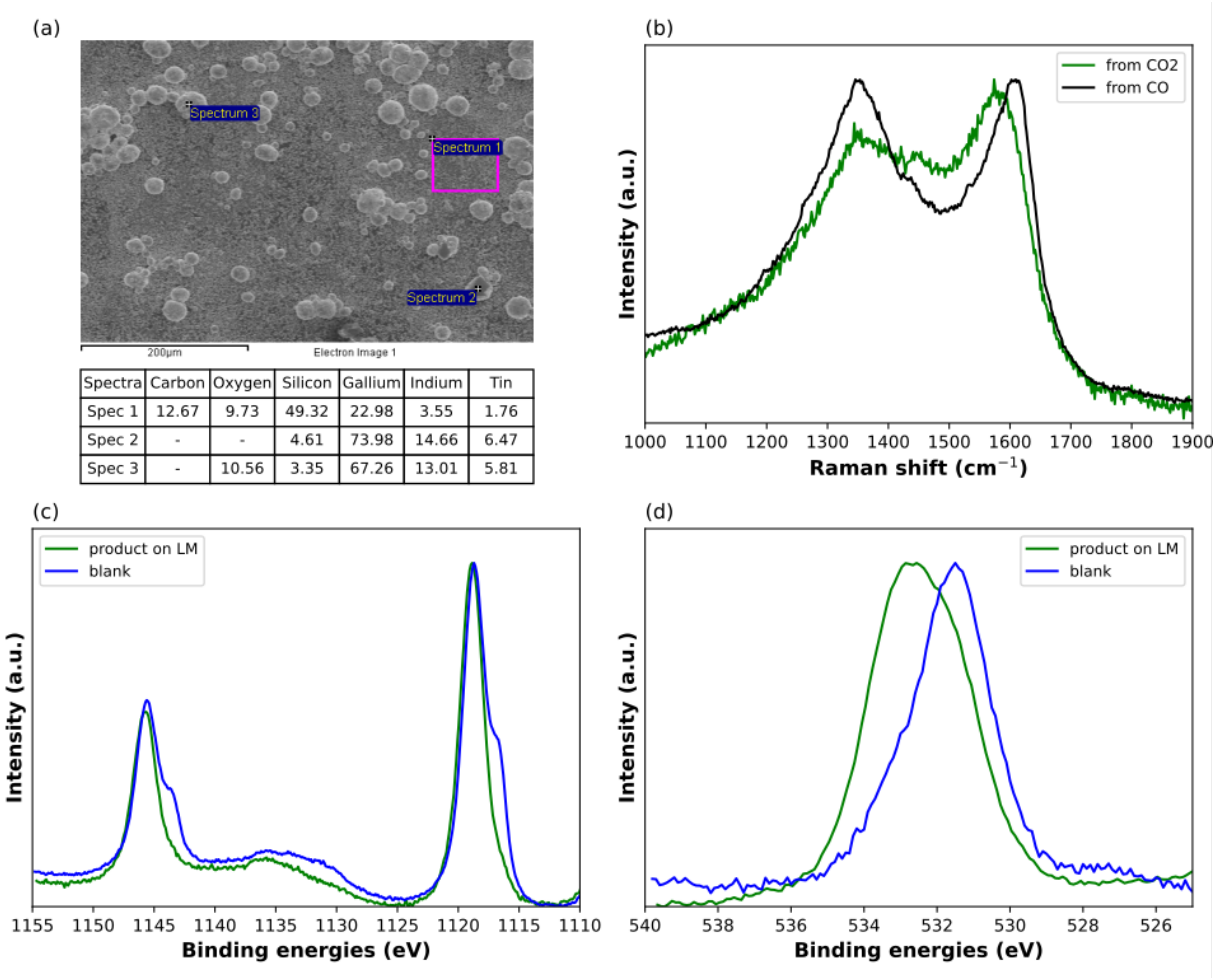

Spectra	Carbon	Oxygen	Silicon	Gallium	Indium	Tin
Spec 1	12.67	9.73	49.32	22.98	3.55	1.76
Spec 2	-	-	4.61	73.98	14.66	6.47
Spec 3	-	10.56	3.35	67.26	13.01	5.81

Figure 4: Characterisation of the solid product based on (a) SEM/EDX, (b) Raman spectroscopy and (c)/(d) XPS spectra of the separated black products' Ga 2p and O 1s signals for the pristine LM (blue) before electrochemistry and the separated top layer with product after CO_2 reduction (green).

Raman spectra (Fig. 4b) were taken for the solid product formed during experiments with CO_2 as purging gas (green) as well as for the product formed when purging with CO (black). Both spectra show pronounced signals at 1605 cm^{-1} (CO)/ 1580 cm^{-1} (CO_2) and 1355 cm^{-1}, that correspond to the characteristic G- and D-band modes well-known for graphitic carbon, thus allowing the conclusion, that in both cases the solid, carbon-rich product is at least partly graphitic.[33,34]

XPS analysis of the product shows that it contains small amounts of cerium, which are not observed by EDX. This is either a consequence of the EDX detection limit or otherwise may point to an exclusive presence of Ce in the uppermost layers of the product sample. Furthermore, the Ce 3d signal in XPS indicates that the cerium is exclusively present in the Ce(III) state as depicted in Fig. 5.

Table 2: Atomic ratios of the metals composing the residual GaInSn that could not be separated from the product.

Ratios	acc.to datasheet	Spectrum 1 (C-rich)	Spectrum 2	Spectrum 3
Ga/In	5.19	6.47	5.05	5.17
Ga/Sn	11.70	13.05	10.98	11.58
In/Sn	2.22	2.02	2.18	2.24

Since the GaInSn remainders/residues in the product with the composition given in Figure 4 hail from the the uppermost layers of the electrochemically cycled GaInSnCe droplet, the shift in atomic ratio points towards an accumulation processes and thus an elemental composition at the catalyst/electrolyte interface that deviates from the bulk composition of the GaInSn-Ce alloy. Such a potential-induced accumulation may lead to an energetically more favourable surface configuration, similar to the process described for eutectic GaIn, in which In is significantly enriched at the GaIn surface.[35] An In/Sn enrichment at the surface might explain the relatively high FE towards formate (Tab. 1) since – unlike gallium – they have been reported to be active catalysts for the production of formic acid in aprotic solvents with low amounts of H_2O.[35–37] The over-representation of gallium coinciding with the presence of graphitic carbon might also point towards a decisive role of gallium in the formation process of the graphitic carbon that is then further catalysed by the presence of cerium. In this case, the over-representation on In and Sn in the non-graphitic regions of the EDX sample might be observed as the counterpart to the depletion of gallium during the C-formation. As only the Ga/Sn ratio shifts in favour of Sn for the non-graphitic sample area, while the In/Sn ratio remains as it was, the Ga-depletion due to an involvement in the graphite formation pathway seems more likely.

The Raman spectra of the product hailing from the CO_2 experiments show a G-band that is shifted towards lower wavenumbers, while the D-band is less pronounced than its counterpart from the CO experiment. As the shift in G-band can be correlated to a higher amount of sp^3-hybridised carbon, while a higher intensity of the D-band is usually linked to larger defect concentrations in the graphite structure, it can be concluded that the product that formed from the purged CO_2 is less defectuous and likely less oxidised than the carbon produced from CO.[33] Tuinstra and Koenig[38] explain a shift of the G-Band from $1575\,cm^{-1}$ towards higher wavenumbers with smaller graphite structures, thus the observed high wavenumber in case of the CO experiments ($1605\,cm^{-1}$) supports the observation of smaller dimensions and limited growth of the graphitic product if CO_2 is absent.

Catalyst properties

To qualitatively assess the composition of the catalyst and possible interface reactions, we investigated the LM-Ce alloy prior to and after the electrochemistry by ex-situ XPS (Figures 4 and 5). The Ga 2p signals (Figure 4c) stemming from the LM matrix indicate that within the information depth of XPS, the gallium is largely oxidised to Ga_2O_3 after the formation of the solid product (green curve), while for the freshly prepared alloy (blue curve), the signal contribution of metallic Ga is more pronounced, probably stemming from sub-surface. For the Ce metal reference sample (grey curves in Figure 5), we observe a pronounced peak in the Ce 3d region at 918.2 eV, which lies in the region typical for CeO_2.[39] This also agrees with the observation of a strong contribution at 530.4 eV to the O 1s signal, while we assign peak components of the other samples around 531.8 eV to the gallium oxide.[40] Yet this region, one would also expect In and Sn oxide species,[41,42] which might, however, not occur on the surface in their bulk concentration due to a potential-induced accumulation of for instance In.[35] Consequently, a deconvolution of the O 1s with respect to Ce species is not feasible here due to the low concentration of Ce in the LM matrix.

The spectra of the Ce 3d orbital of the LM matrix samples in Figure 5(a) show doublet-

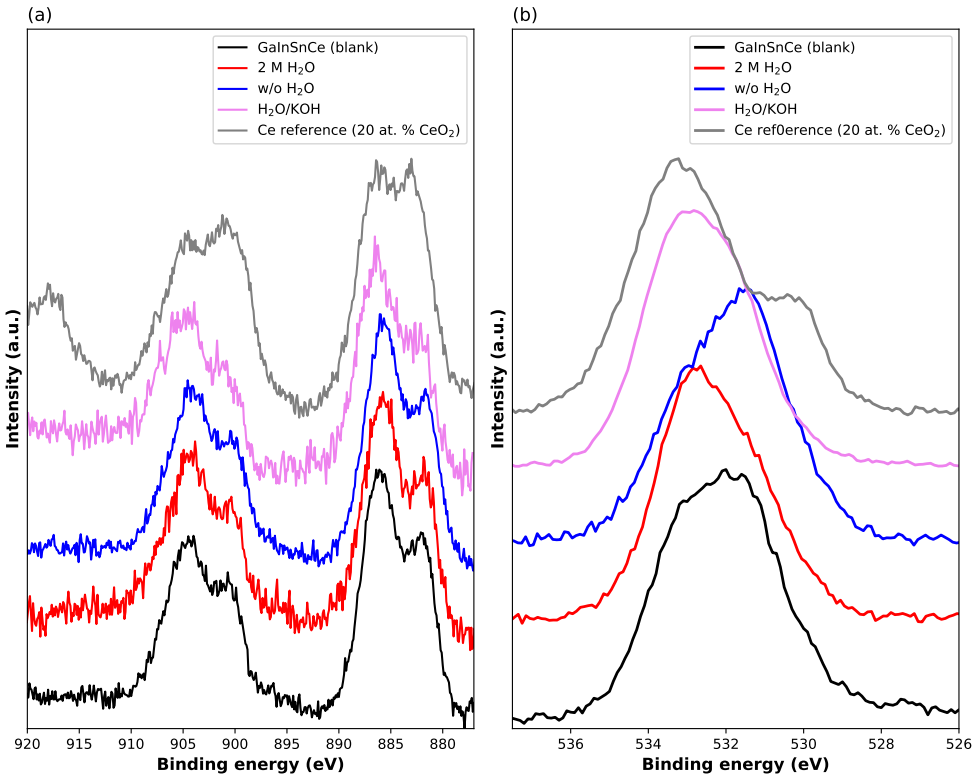

Figure 5: XPS analysis of the GaInSnCe alloy before and after before and after CA measurements for the three different experimental conditions (without additional H_2O (blue), with 2 M H_2O (red curve), and with 2 M H_2O of pH=12 (pink)) compared to two references, Ce metal (grey), and the Ce-alloy before exposure to the electrolyte (black). (a) Ce 3d spectra and (b) O 1s spectra.

peaks with their main signal at ~886 eV (Ce $3d_{5/2}$) and ~904.6 eV (Ce $3d_{3/2}$), which is good agreement with literature values for Ce_2O_3.[39,43] This is in contrast to the previously stated hypothesis, that CeO_2 is involved in the catalytic process.[9] The presence of CeO_2 would be observable by the occurrence of the peak at 918.2 eV (see reference sample, grey curve). We therefore conclude that for the alloyed LM-Ce, the surface cerium is present as cerium(III) oxide (Ce_2O_3) with no observable contributions of cerium(IV) oxide (CeO_2).

Strictly speaking, this statement is only valid for the catalyst before and after the electrochemistry and does not necessarily reflect its operando state. However, as CeO_2 is considered the most stable configuration of cerium at ambient conditions,[31] it can be deduced that CeO_2 does most likely not contribute to the catalytic process, as residues, that have not yet been

reduced during the oxygen stripping of CO_2 or CO, would be stable even in ambient conditions and would not be converted back to the cerium(III) oxide. Thus, a missing signal of Ce(IV) oxide in the ex-situ XPS analysis makes the presence of Ce(IV) under operation conditions highly unlikely unless this species is a reaction intermediate. The latter could explain, why Ce-O-Ce was found with operando Raman under very cathodic potentials.[9]

In the case of controlled amounts of H_2O being added to the electrolyte solution, it can be observed that the contribution to the O 1s signal at 533 eV increases by at least a factor of 3 in intensity compared to the sample exposed to the dry electrolyte, while the latter shows by far the strongest contribution of the component at 531.8 eV. Thus the increase in 533 eV appears to be linked to the increased occurrence of cerium hydroxide and other hydroxides.

These findings from XPS can now be linked to the observation that the process leading to the formation of graphitic flakes is significantly accelerated in OH-rich electrolyte solution and seemingly non-existent if cerium is missing in the alloy. This suggests that OH-terminated surface cerium or a thin layer of $Ce(OH)_x$ is important for the electrocatalytic activity for the reduction of CO_2 to graphitic carbon.

Reaction mechanism

From these experimental results, it is now possible to outline a potential reaction pathway for the CO_2 reduction on the LM-Ce alloy to solid carbon species. Qualitatively, the production of solid carbon species – graphitic carbon with a certain degree of amorphous components similar to carbon black[44] – is independent of the presence of (dilute) H_2O, while the presence of Ce is a prerequisite for the formation of this product. The production rate is, however, drastically enhanced in the presence of KOH. This could indicate that the catalytically active Ce(III) species are stabilised by OH groups/$Ce(OH)_3$ or even that the latter is the active species. This is in line with the findings of Wang et al.[30] who propose cerium(III) as active centres for C-deposition processes. As furthermore, the availability of acid sites seems crucial to carbon deposition processes, the importance of the stabilisation of a Ce(III) species

instead of Ce(0) is additionally emphasised.[45] CO appears to be a reaction intermediate, but not sufficient for the formation of larger carbon flakes, as the solid product forms more quickly with only CO added to the solution, but the process appears to come to a stop at low total yield if no CO_2 is present in the solution. As Grebenko et al.[46] have described, graphene growth based on CO as the carbon source suffers from a self-limiting effect due to facilitated CO adsorption at the propagation front of the graphene nuclei in comparison to the catalyst surface, where CO dissociates into new building blocks. Thus the subsequent lateral attachment of graphene precursors is kinetically hindered. Small amounts of CO_2 already seem to have a sufficiently strong etching effect on these growth-limiting CO at the graphene edges, hereby allowing the layer growth to continue.[47] This would explain the restricted growth rate we observe when using CO as the purging gas in comparison to CO_2.

The by about 40% lower solubility of CO compared to CO_2 in the DMF/H_2O mixture might also affect the formation rate of the solid carbon product, yet it would not sufficiently explain the higher solid product formation rate in case of CO_2 being present.[48,49]

As the LM surface changes its stoichiometry during the reaction towards a slight Ga accumulation when compared to In and Sn, a significant role of gallium for the observed formation of graphitic carbon seems likely. Ga-species could play the role of catalysing the conversion from CO_2 to CO,[50] while In and Sn species are likely to additionally produce formate and hydrogen in the presence of water.[36] Hereby, a mixture of CO/CO_2 would be created at low temperatures. Meanwhile the LM surface bears cerium(III) catalytic centres due to the alkaline H_2O, that are stable at highly cathodic potentials and are furthermore highly mobile due to the liquid nature of its "substrate". This seems to lead to ideal conditions for the sustained growth of graphitic carbon – in contrast to initial, but limited deposition of poorly ordered graphene observed for many metals.[51]

At this stage, one could imagine two main reaction pathways from CO_2 to C that have already been discussed in the literature. In a Boudouard-type reaction, C is formed from two CO molecules $2CO(g) \rightarrow C(s) + CO_2(g)$, while the reverse water gas shift reaction involves

hydrogen: $CO(g) + H_2(g) \rightarrow C(s) + H_2O(g)$.[45] As the Boudouard reaction is hindered by the availability of water, while we find higher C formation rates in the presence of H_2O, the latter of the two appears to be more likely here.

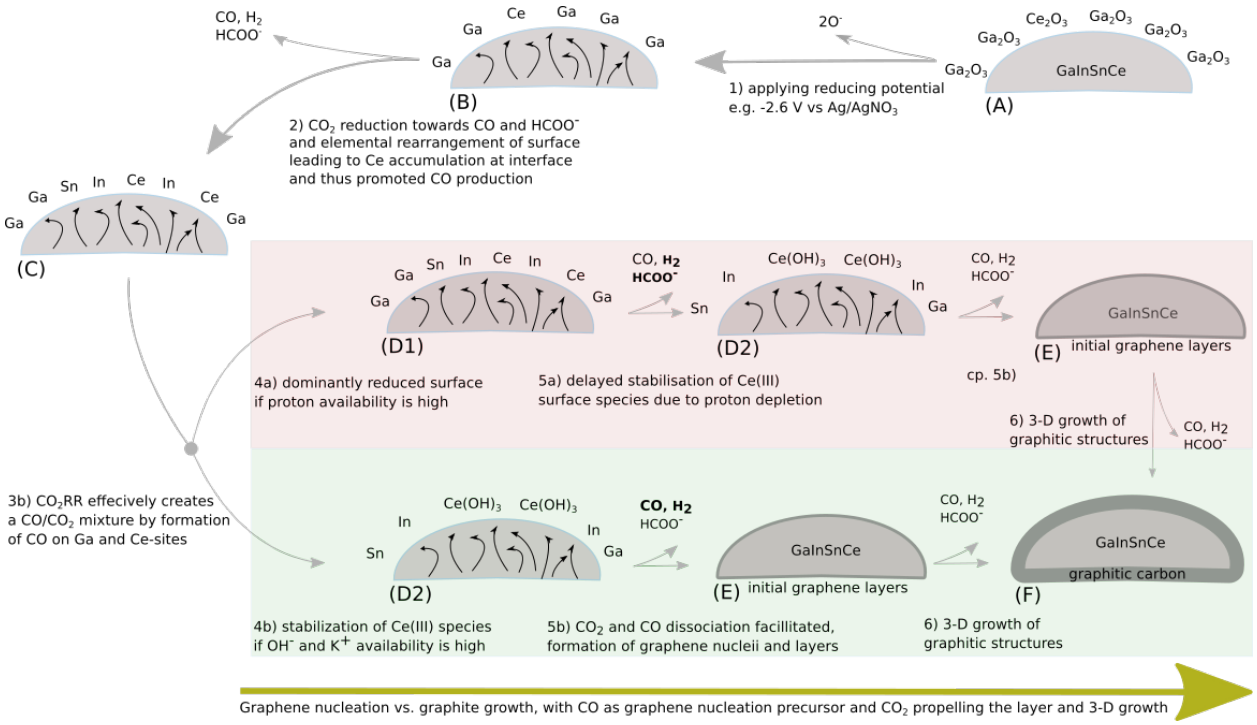

Figure 6: Proposed scheme for the overall reaction pathway to solid carbon, indicating the surface composition of the LM droplet in CO_2-purged electrolyte (not shown). Large grey arrows between the steps from (A) to (F) denote changes in surface composition, small grey arrows the evolved products. The colorisation of the backdrop indicates high (green) and low (red) formation rate of the graphitic carbon product.

In Figure 6, we propose an overall scheme for the reaction mechanism that is compatible with our observations: (A) The GaInSnCe surface with its Ga-dominated native oxide layer is reduced at cathodic potentials of at least -2 V vs. $Ag/AgNO_3$ to create a fully reduced metallic surface (B). In the presence of CO_2, reduction reactions towards CO and (if H_2O is present) towards formate and hydrogen are occurring. At the same time, a potential-driven segregation process takes place, which changes the surface composition and leads to an accumulation of Ce on the surface of the alloy (C). Depending on the availability of OH^- and – potentially – the presence of K^+, the formation of graphitic structures appears to be significantly accelerated. While the presence of OH^- and K^+ may lead to the immediate

stabilisation of catalytically more beneficial surface structures like $Ce(OH)_3$ (D2), the formation of those species might be delayed in case of the usage of neutral H_2O in the electrolyte solution (D1). If pure H_2O is present, the formation of hydrogen and formate may lead to a local depletion of protons which could gradually create an environment similar to the one stated above and thus stabilise $Ce(OH)_3$ with a certain delay. The CO – which is supposedly dominantly produced at Ga and Ce-sites – is captured by the Ce(III) surface species, the oxygen is split off. In the following, a cyclisation process with multiple of likewise-produced, surface-bound C-species takes place, forming graphene nuclei (E). Subsequently, a growth process proceeds that seems to be facilitated in the presence of CO_2, but not CO, which ultimately leads to the exfoliation of graphitic carbon from the otherwise fully covered GaInSnCe surface (F).

To test our hypothesis on the interplay between water, OH, Ce, and the CO_2 molecule, we modelled the dissociation of CO_2 on a Ce metal surface by DFT (Fig. 7). The calculations of the CO_2 reduction towards carbon show a high reactivity of the Ce metal surface with the overall process being thermodynamically favourable (Fig. 8). In fact, both reaction steps from CO_2 to CO and from CO to C result in a decrease in energy.

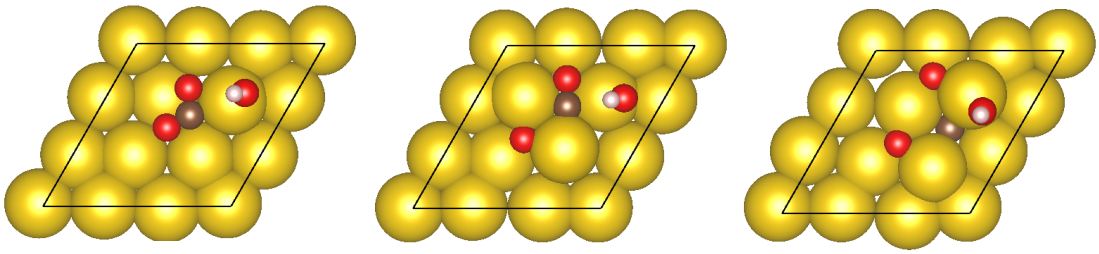

Figure 7: Dissociation of CO_2 on the Ce(111) surface in the presence of a co-adsorbed OH group. Initial and final states of the two dissociation steps (CO_2 to CO and CO to C) are depicted from left to right.

Thus, Ce metal can in principle reduce CO_2. It has to be pointed out that the CO_2 molecule adsorbs in a bent geometry (see Fig. 7), which is indicative for the activation of the molecule. To resolve the question of reaction path and activation energy, the kinetics of the outlined reduction steps has been analysed by the nudged elastic band (NEB) method.[52,53]

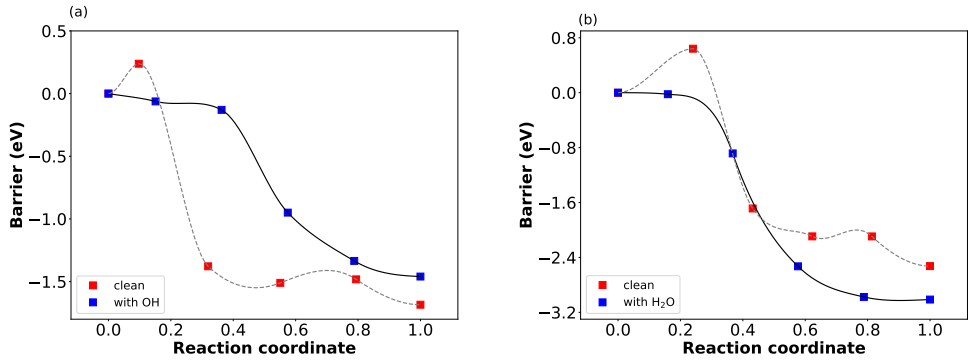

Figure 8: Dissociation barriers (a) for the first (CO_2 to CO, eq. 1) and (b) for the second (CO to C, eq. 2) reaction step with and without the presence of a co-adsorbed OH group.

For this purpose, the activation barriers for both reaction steps, from CO_2 to CO and from CO to C, were computed. The observed barriers amount to 0.24 and 0.64 eV, respectively, thus making the second step the rate-determining one (see Fig. 8). As the experimental findings indicated a positive impact of alkaline conditions, a next step was to investigate the just discussed reaction steps in the presence of small amounts of OH and trace water (see SI for the latter). This was mimicked by placing a single OH group (water molecule) on the surface. Here, it has to be pointed out that a 1 molar solution of water in an organic electrolytes means an average distance of ∼10 Å between water molecules. This means that considering only one co-adsorbed OH group (water molecule) on the investigated surface is indeed rather close to the experimental conditions. Interestingly, the thermodynamics of the reaction is only slightly changed by the nearby molecules. However, in the case of the co-adsorbed OH group, as well as for a co-adsorbed water molecule, the reaction barriers disappear (see Fig. 8 and Fig. S2) for both reaction steps, which is more pronounced in the case of OH. This may be attributed to the interaction of CO_2 (CO) with the dipole moment of the adsorbed molecules. Consequently, one would expect this to be observed only for trace amounts of water and OH, as the impact of larger water concentrations, in particular for the case of water, would be expected to average out. Regarding the reaction mechanism, this complete dissociation of CO_2 to adsorbed C and O without barrier then requires the desorption of an O species from the Ce and transport thereof to the counter-electrode, where

the oxidation reaction takes place. This could take place in the form of hydroxide which is then oxidised to O_2 at the counter-electrode, which further emphasises the importance of water in the overall process. From this DFT model, one could derive the following reaction scheme under the assumption that $Ce(OH)_x$ is present in small clusters on the surface of the LM matrix, where equations 1-3 take place on the cathode in the vicinity of an adsorbed OH group (Ce-OH), and equation 4 on the anode:

$$CO_2 + 2Ce \rightarrow CO + Ce{-}O + Ce \quad (1)$$

$$CO + Ce{-}O + 2Ce \rightarrow 2(Ce{-}O) + Ce{-}C \quad (2)$$

$$Ce{-}O + H_2O + 2e^- \rightarrow Ce + 2OH^- \quad (3)$$

$$4OH^- + 4h^+ \rightarrow O_2 + 2H_2O \quad (4)$$

With respect to the build-up of graphitic carbon, different growth mechanisms seem to be possible. A chain-like mechanism with subsequent chain-linking as suggested by Keller et al.[31] could be imagined.

Conclusion

In summary, we have explored catalyst synthesis, active species, and reaction mechanism of a Ce-alloyed liquid metal matrix for the electroreduction of CO_2 to solid carbon species. For the synthesis, we have found that the incorporation of (large) Ce particles freshly produced from Ce metal combined with pre-conditioning of the grinding mortar result in a catalyst that reliably produces graphitic carbon from CO_2. Unlike stated in the literature, we find that Ce(III) oxide species, stabilised by OH-termination or a surface $Ce(OH)_x$ phase, is the catalytically active species. While the presence of small quantities of H_2O generally increases cathodic currents and the formation of H-containing products such as formate,

a higher alkalinity benefits the solid product yield. The reaction mechanism appears to also involve CO as an intermediate species, while CO_2 promotes the growth of the solid into larger flakes followed by exfoliation, preventing catalyst deactivation. Our results are supported by calculations from density functional theory, finding that especially the presence of OH-groups on the Ce surface lead to the almost complete disappearance of the reaction barrier for splitting off both oxygen atoms from CO_2. The next step towards practical electrochemical CO_2 reduction to solid carbon for carbon dioxide removal will now be to use this improved understanding to increase faradaic efficiencies of the catalyst for graphitic carbon sink product.

Acknowledgement

This work was funded by the German Research Foundation (DFG) under project number 434023472 and the German Bundesministerium für Bildung and Forschung (BMBF), project "NETPEC" (No. 01LS2103A and 01LS2103B). The authors acknowledge support by the state of Baden-Württemberg through bwHPC and the German Research Foundation (DFG) through grant no INST 40/575-1 FUGG (JUSTUS 2 cluster). Part of the simulations were performed on the national supercomputer Hawk at the High Performance Computing Center Stuttgart (HLRS) under the grant number SPECSY/44227. The authors thank Markus Maisch for lab support and Heiko Peisert for access to XPS as well as Eric Juriatti and Philipp Haizmann for technical XPS support.

Data availability

The data underlying this study will be made openly available upon publication on Zenodo.[54]

Supporting Information Available

The following files are available free of charge.

- SupportingInformation.pdf: Additional experimental figures as well as DFT results in the presence of water.

References

(1) Hansen, J.; Sato, M.; Kharecha, P.; von Schuckmann, K.; Beerling, D. J.; Cao, J.; Marcott, S.; Masson-Delmotte, V.; Prather, M. J.; Rohling, E. J. et al. Young people's burden: requirement of negative CO_2 emissions. *Earth Syst. Dyn.* **2017**, *8*, 577–616.

(2) Lamboll, R. D.; Nicholls, Z. R. J.; Smith, C. J.; Kikstra, J. S.; Byers, E.; Rogelj, J. Assessing the size and uncertainty of remaining carbon budgets. *Nat. Clim. Change* **2023**, *13*, 1360–1367.

(3) Smith, P.; Davis, S. J.; Creutzig, F.; Fuss, S.; Minx, J.; Gabrielle, B.; Kato, E.; Jackson, R. B.; Cowie, A.; Kriegler, E. et al. Biophysical and economic limits to negative CO_2 emissions. *Nat. Clim. Change* **2016**, *6*, 42–50.

(4) Rau, G. H. The race to remove CO_2 needs more contestants. *Nat. Clim. Change* **2019**, *9*, 256.

(5) Heck, V.; Gerten, D.; Lucht, W.; Popp, A. Biomass-based negative emissions difficult to reconcile with planetary boundaries. *Nat. Clim. Change* **2018**, *8*, 151–155.

(6) May, M. M.; Rehfeld, K. ESD Ideas: Photoelectrochemical carbon removal as negative emission technology. *Earth Syst. Dyn.* **2019**, *10*, 1–7.

(7) May, M. M.; Rehfeld, K. Negative emissions as the new frontier of photoelectrochemical CO_2 reduction. *Adv. Energy Mater.* **2022**, *12*, 2103801.

(8) van de Krol, R.; Parkinson, B. A. Perspectives on the photoelectrochemical storage of solar energy. *MRS Energy Sust.* **2017**, *4*, 13.

(9) Esrafilzadeh, D.; Zavabeti, A.; Jalili, R.; Atkin, P.; Choi, J.; Carey, B. J.; Brkljača, R.; O'Mullane, A. P.; Dickey, M. D.; Officer, D. L. et al. Room temperature CO_2 reduction to solid carbon species on liquid metals featuring atomically thin ceria interfaces. *Nat. Commun.* **2019**, *10*, 865.

(10) Irfan, M.; Zuraiqi, K.; Nguyen, C. K.; Le, T. C.; Jabbar, F.; Ameen, M.; Parker, C. J.; Chiang, K.; Jones, L. A.; Elbourne, A. et al. Liquid metal-based catalysts for the electroreduction of carbon dioxide into solid carbon. *J. Mater. Chem. A* **2023**, *11*, 14990–14996.

(11) Ye, L.; Syed, N.; Wang, D.; Murdoch, B. J.; Zuraqi, K.; Alivand, M. S.; Xiao, P.; Singh, R.; Zu, L.; Mumford, K. A. et al. CO_2 reduction on the Li–Ga liquid metal surface. *J. Mater. Chem. A* **2023**, *11*, 8809–8816.

(12) Sun, X.; Li, H. Recent progress of Ga-based liquid metals in catalysis. *RSC Adv.* **2022**, *12*, 24946–24957.

(13) Daeneke, T.; Khoshmanesh, K.; Mahmood, N.; de Castro, I. A.; Esrafilzadeh, D.; Barrow, S. J.; Dickey, M. D.; Kalantar-zadeh, K. Liquid metals: fundamentals and applications in chemistry. *Chem. Soc. Rev.* **2018**, *47*, 4073–4111.

(14) Handschuh-Wang, S.; Gan, T.; Rauf, M.; Yang, W.; Stadler, F. J.; Zhou, X. The subtle difference between Galinstan (R) and eutectic GaInSn. *Materialia* **2022**, *26*, 101642.

(15) Handschuh-Wang, S.; Zhu, L.; Gan, T.; Wang, T.; Wang, B.; Zhou, X. Interfacing of surfaces with gallium-based liquid metals – approaches for mitigation and augmentation of liquid metal adhesion on surfaces. *Appl. Mater. Today* **2020**, *21*, 100868.

(16) Tang, S.-Y.; Sivan, V.; Khoshmanesh, K.; O'Mullane, A. P.; Tang, X.; Gol, B.; Eshtiaghi, N.; Lieder, F.; Petersen, P.; Mitchell, A. et al. Electrochemically induced actuation of liquid metal marbles. *Nanoscale* **2013**, *5*, 5949–5957.

(17) Chen, S.; Yang, X.; Cui, Y.; Liu, J. Self-growing and serpentine locomotion of liquid metal induced by copper ions. *ACS Appl. Mater. Interfaces* **2018**, *10*, 22889–22895.

(18) Abràmoff, M. D.; Magalhães, P. J.; Ram, S. J. Image processing with ImageJ. *Biophotonics Int.* **2004**, *11*, 36–42.

(19) Kresse, G.; Hafner, J. Ab-initio molecular dynamics for liquid metals. *Phys. Rev. B* **1993**, *47*, 558–561.

(20) Kresse, G.; Furthmüller, J. Efficient iterative schemes for ab initio total-energy calculations using a plane-wave basis set. *Phys. Rev. B* **1996**, *54*, 11169–11186.

(21) Hammer, B.; Hansen, L. B.; Nørskov, J. K. Improved adsorption energetics within density-functional theory using revised Perdew-Burke-Ernzerhof functionals. *Phys. Rev. B* **1999**, *59*, 7413–7421.

(22) Grimme, S.; Antony, J.; Ehrlich, S.; Krieg, H. A consistent and accurate ab initio parametrization of density functional dispersion correction (DFT-D) for the 94 elements H-Pu. *J. Chem. Phys.* **2010**, *132*, 154104.

(23) Creager, S. In *Handbook of Electrochemistry*; Zoski, C. G., Ed.; Elsevier: Amsterdam, 2007; pp 57–72.

(24) Dahm, C. E.; Peters, D. G. Electrochemical reduction of tetraalkylammonium tetrafluoroborates at carbon cathodes in dimethylformamide. *J. Electroanal. Chem.* **1996**, *402*, 91–96.

(25) Eggins, B. R.; Brown, E. M.; McNeill, E. A.; Grimshaw, J. Carbon dioxide fixation by

electrochemical reduction in water to oxalate and glyoxylate. *Tetrahedron Lett.* **1988**, *29*, 945–948.

(26) Fejzic, H.; Kumar, R.; Gomes, R.; He, L.; Houser, T.; Kim, J.; Molten, N.; Amanchukwu, C. Water clustering modulates activity and enables hydrogenated product formation during carbon monoxide electroreduction in aprotic media. *ChemRxiv* **2024**,

(27) Kobara, H.; Wakisaka, A.; Takeuchi, K.; Ibusuki, T. Preferential solvation of Na+ in N,N-dimethylformamide-water binary mixture. *J. Phys. Chem. B* **2003**, *107*, 11827–11829.

(28) Liu, X.; Wang, S.; Xu, X.; Khair, H.; Dong, Z.; Wang, H.; Zhang, W.; Yu, T.; Men, Z.; Sun, C. et al. Exploring the dynamic changes in hydrogen bond structure of water and heavy water under external perturbation of DMF. *Spectrochim. Acta Part A Mol. Biomol. Spectrosc.* **2024**, *305*, 123493.

(29) Bai, Y.; Zhou, D.; Mukherjee, S.; Liu, J.; Bian, H.; Fang, Y. Distinct hydrogen bonding dynamics underlies the microheterogeneity in DMF–water mixtures. *J. Phys. Chem. B* **2022**, *126*, 9663–9672, PMID: 36351006.

(30) Wang, J.; Bishop, S. R.; Sun, L.; Lu, Q.; Vardar, G.; Bliem, R.; Tsvetkov, N.; Crumlin, E. J.; Gallet, J.-J.; Bournel, F. et al. Threshold catalytic onset of carbon formation on CeO_2 during CO_2 electrolysis: mechanism and inhibition. *J. Mater. Chem. A* **2019**, *7*, 15233–15243.

(31) Keller, F.; Döhn, J.; Groß, A.; Busch, M. Exploring the mechanism of the electrochemical polymerization of CO_2 to hard carbon over CeO_2(110). *J. Phys. Chem. C* **2024**, *128*, 6280–6293.

(32) Gao, D.; Arán-Ais, R. M.; Jeon, H. S.; Cuenya, B. R. Rational catalyst and electrolyte

design for CO_2 electroreduction towards multicarbon products. *Nat. Catal.* **2019**, *2*, 198–210.

(33) Dychalska, A.; Popielarski, P.; Franków, W.; Fabisiak, K.; Paprocki, K.; Szybowicz, M. Study of CVD diamond layers with amorphous carbon admixture by raman scattering spectroscopy. *Mater. Sci.-Pol.* **2015**, *33*.

(34) Perumbilavil, S.; Sankar, P.; Priya Rose, T.; Philip, R. White light Z-scan measurements of ultrafast optical nonlinearity in reduced graphene oxide nanosheets in the 400–700 nm region. *Appl. Phys. Lett.* **2015**, *107*, 051104.

(35) Gholampoursaadi, F.; Zhi, X.; Nour, S.; Liu, J. Z.; Li, G. K.; Mayyas, M. Surface enrichment in gallium-indium liquid alloys: Applied to CO_2 conversion. *Adv. Funct. Mater.* **2024**, 2316435.

(36) Ikeda, S.; Takagi, T.; Ito, K. Selective formation of formic acid, oxalic acid, and carbon monoxide by electrochemical reduction of carbon dioxide. *Bull. Chem. Soc. Jpn.* **2006**, *60*, 2517–2522.

(37) Hori, Y. In *Modern aspects of electrochemistry*; Vayenas, C. G., White, R. E., Gamboa-Aldeco, M. E., Eds.; Springer New York: New York, NY, 2008; pp 89–189.

(38) Tuinstra, F.; Koenig, J. L. Raman spectrum of graphite. *J. Chem. Phys.* **1970**, *53*, 1126–1130.

(39) Anandan, C.; Bera, P. XPS studies on the interaction of CeO_2 with silicon in magnetron sputtered CeO_2 thin films on Si and Si_3N_4 substrates. *Appl. Surf. Sci.* **2013**, *283*, 297–303.

(40) Mulazzi, M.; Reichmann, F.; Becker, A.; Klesse, W. M.; Alippi, P.; Fiorentini, V.; Parisini, A.; Bosi, M.; Fornari, R. The electronic structure of ϵ-Ga_2O_3. *APL Mater.* **2019**, *7*, 022522.

(41) Šeruga, M.; Metikoš-Huković, M.; Valla, T.; Milun, M.; Hoffschultz, H.; Wandelt, K. Electrochemical and X-ray photoelectron spectroscopy studies of passive film on tin in citrate buffer solution. *J. Electroanal. Chem.* **1996**, *407*, 83–89.

(42) May, M. M.; Lewerenz, H.-J.; Hannappel, T. Optical in situsStudy of InP(100) surface Chemistry: Dissociative Adsorption of Water and Oxygen. *J. Phys. Chem. C* **2014**, *118*, 19032–19041.

(43) Mullins, D.; Overbury, S.; Huntley, D. Electron spectroscopy of single crystal and polycrystalline cerium oxide surfaces. *Surf. Sci.* **1998**, *409*, 307–319.

(44) Bokobza, L.; Bruneel, J.-L.; Couzi, M. Raman Spectra of Carbon-Based Materials (from Graphite to Carbon Black) and of Some Silicone Composites. *C* **2015**, *1*, 77–94.

(45) Boldrin, P.; Ruiz-Trejo, E.; Mermelstein, J.; Bermúdez Menéndez, J. M.; Ramírez Reina, T.; Brandon, N. P. Strategies for carbon and sulfur tolerant solid oxide fuel cell materials, incorporating lessons from heterogeneous catalysis. *Chem. Rev.* **2016**, *116*, 13633–13684.

(46) Grebenko, A. K.; Krasnikov, D. V.; Bubis, A. V.; Stolyarov, V. S.; Vyalikh, D. V.; Makarova, A. A.; Fedorov, A.; Aitkulova, A.; Alekseeva, A. A.; Gilshtein, E. et al. High-quality graphene using boudouard reaction. *Adv. Sci.* **2022**, *9*, 2200217.

(47) Kim, H.; Mattevi, C.; Calvo, M. R.; Oberg, J. C.; Artiglia, L.; Agnoli, S.; Hirjibehedin, C. F.; Chhowalla, M.; Saiz, E. Activation energy paths for graphene nucleation and growth on Cu. *ACS Nano* **2012**, *6*, 3614–3623.

(48) Khan, M. M. T.; Halligudi, S. B.; Shukla, S. Solubility of carbon monoxide in water-n-butylamine, ethanol-cyclohexene and water-dimethylformamide mixtures. *J. Chem. Eng. Data* **1989**, *34*, 353–355.

(49) Jödecke, M.; Pérez-Salado, A.; Maurer, G. An experimental investigation of the solubility of CO_2 in (N,N-dimethylmethanamide + water). *J. Chem. Eng. Data* **2012**, *57*, 1249–1266.

(50) Kuntyi, O.; Zozulya, G.; Shepida, M. CO_2 electroreduction in organic aprotic solvents: A mini review. *J. Chem.* **2022**, *2022*, 1306688.

(51) Bartelt, N.; McCarty, K. Graphene growth on metal surfaces. *MRS Bull.* **2012**, *37*, 1158–1165.

(52) Jónsson, H.; Mills, G.; Jacobsen, K. W. Nudged elastic band method for finding minimum energy paths of transitions. *Class. Quantum Dyn. Condens. Phase Simulations - Proc. Int. Sch. Phys.* **1998**, 385–404.

(53) Henkelman, G.; Uberuaga, B. P.; Jónsson, H. A climbing image nudged elastic band method for finding saddle points and minimum energy paths. *J. Chem. Phys.* **2000**, *113*, 9901.

(54) Lörch, D.; Mohamed, A. G. A.; Euchner, H.; Timm, J.; Hiller, J.; Bogdanoff, P.; May, M. M. Dataset for "From CO_2 to solid carbon: reaction mechanism, active species, and conditioning the Ce-alloyed GaInSn catalyst". 2024.

TOC Graphic